Maruyama *et al. Earth, Planets and Space* (2017) 69:20
DOI 10.1186/s40623-017-0600-z

Earth, Planets and Space

FULL PAPER

Open Access

Sensitivity of ionosonde detection of atmospheric disturbances induced by seismic Rayleigh waves at different latitudes

Takashi Maruyama[1,2*], Hiroyuki Shinagawa[1], Kamil Yusupov[2] and Adel Akchurin[2]

Abstract

Ionospheric disturbance was observed in ionograms at Kazan, Russia (55.85°N, 48.81°E), associated with the M8.8 Chile earthquake in 2010 (35.91°S, 72.73°W). The disturbance was caused by infrasound waves that were launched by seismic Rayleigh waves propagating over 15,000 km along Earth's surface from the epicenter. This distance was extremely large compared with the detection limit of similar ionospheric disturbances that were previously studied at lower latitudes over Japan. The observations suggest that the sensitivity of ionograms to coseismic atmospheric disturbances in the infrasound range differs at different locations on the globe. A notable difference in the geophysical condition between the Russian and Japanese ionosonde sites is the magnetic inclination (dip angle), which affects the ionosphere–atmosphere dynamical coupling and radio propagation of vertical incidence ionosonde sounding. Numerical simulations of atmospheric–ionospheric perturbation were conducted, and ionograms were synthesized from the disturbed electron density profiles for different magnetic dip angles. The results showed that ionosonde sounding at Kazan was sensitive to the atmospheric disturbances induced by seismic Rayleigh waves compared with that at Japanese sites by a factor of ∼3.

Keywords: Ionosonde, Earthquakes, Rayleigh waves, Infrasound, Lithosphere–atmosphere–ionosphere coupling

Background

Large earthquakes are known to cause appreciable ionospheric disturbances through lithosphere–atmosphere–ionosphere coupling. The vertical ground motion of seismic waves launches infrasonic acoustic waves (infrasound) into the atmosphere, and the excited waves propagate upward. The amplitude of waves increases with height owing to conservation of momentum, because the atmosphere is rarefied exponentially with height. The neutral particle motion of the acoustic waves induces alternating enhancements and depletions of plasma density through the neutral–ion collisions at ionospheric heights (Maruyama and Shinagawa 2014). The resulting ionospheric perturbation is detected by various radio techniques. The trans-ionospheric radio propagation of signals transmitted from Global Positioning Satellite System (GPS) satellites is used to observe the coseismic effect on the total electron content (TEC) along the ray path (Calais and Minster 1995; Tsugawa et al. 2011; Rolland et al. 2011). The Doppler sounding with continuous high-frequency (HF) radio waves detects the periodic fluctuation of phase length associated with the electron density perturbation near the reflection level (Yuen et al. 1969; Wolcott et al. 1984; Tanaka et al. 1984; Artru et al. 2004; Chum et al. 2012, 2016). The pulsed HF radar tracks horizontal propagation of the perturbation (Nishitani et al. 2011; Ogawa et al. 2012). A combination of the TEC measurements, HF Doppler sounding, magnetometer, and ground infrasonic sounder tracks the vertical propagation of the perturbation, since each technique is sensitive to the disturbances at different height (Liu et al. 2016). The vertical incidence radio sounding (ionosonde) observes the distortion of echo traces (Leonard and Barnes 1965; Yuen et al. 1969; Liu and Sun 2011; Maruyama et al. 2011, 2012, 2016a, b; Maruyama and

*Correspondence: tmaru@nict.go.jp
[1] National Institute of Information and Communications Technology, 2-1 Nukuikita 4-chome, Koganei, Tokyo 184-8795, Japan
Full list of author information is available at the end of the article

Shinagawa 2014; Berngardt et al. 2015) and is a technique dealt with in this paper, as described further below.

At remote distances from the epicenter, Rayleigh waves are the most important source of coseismic infrasound because they propagate along Earth's surface without significant attenuation of the amplitude due to geometrical spreading (Lay and Wallace 1995). The ionospheric anomaly exhibits a characteristic of traveling ionospheric disturbances following the Rayleigh wave propagation (Liu and Sun 2011; Maruyama et al. 2012). Short-period Rayleigh waves in the range of 15–50 s, near the Airy phase, yield ionospheric density fluctuations with vertical wavelengths of 7.5–50 km, because the sound speed is 500–1000 m/s at ionospheric heights. The vertical wavelength is less than the bottom-half thickness of the ionosphere, and several cycles of alternating enhancements and depletions of electron density cause distortion of the ionograms characterized as a multiple cusp signature (MCS) (Maruyama et al. 2011, 2016a, b; Maruyama and Shinagawa 2014). Each cusp is related to a density ledge, and the vertical separation of the ledges is the wavelength of the infrasound propagating in the thermosphere (Maruyama et al. 2012, 2016a). Thus, MCS ionograms are considered to be a wave snapshot. Note that this type of ionospheric anomaly is not detected by TEC measurement because the alternating enhancements and depletions of electron density along the ray path offset the contribution to the TEC changes.

Maruyama et al. (2012) examined earthquakes that occurred worldwide with a seismic magnitude of 8.0 or greater and ionograms observed at five ionosonde sites over Japan during the period from 1957 to 2011 and concluded that the detection of MCSs was limited to epicentral distances shorter than ~6000 km. Contrary to this, however, MCSs were observed at several sites in Russia (Kaliningrad and Kazan) and Finland (Sodankylä) with long epicentral distances of 9000–15,000 km after several large earthquakes (Yusupov and Akchurin 2015). One of those events observed at Kazan, Russia, after the M8.8 Chile earthquake in 2010 was examined in detail by Maruyama et al. (2016a, b). A notable difference between Kazan and Japanese ionosonde sites is the inclination of Earth's magnetic field (dip angle) I, i.e., $I = 72°$ at Kazan and $I = 38, 45, 49, 53,$ and $59°$ at Japanese sites (Okinawa, Yamagawa, Kokubunji, Akita, and Wakkanai, respectively). Maruyama et al. (2016a) briefly discussed magnetic inclination effects that potentially affect the sensitivity of ionosondes to upper atmospheric disturbances induced by upward propagating infrasound. Other differences are the topology of Earth's surface and jet streams, which may distort the wave fronts of acoustic waves propagating from the ground to the ionospheric level, but these are outside the scope of the current paper. The magnetic inclination effects are discussed quantitatively in this paper. Here we present numerical simulations of infrasonic acoustic waves and electron density perturbation induced by vertical ground motion of seismic Rayleigh waves. Ionograms were synthesized from the simulated electron density profiles for different dip angles. Examples of MCS ionograms are presented in the next section. Magnetic inclination effects, numerical simulations, and synthetic ionograms follow. The results are summarized in the last section.

Observations

The magnitude 8.8 earthquake occurred offshore of Maule (35.91°S, 72.73°W), Chile, at 0634:14 UTC on February 27, 2010, and seismic signals were recorded at Obninsk (55.11°N, 36.57°E; epicentral distance 14,375 km), Russia, approximately 1 h after the earthquake, as shown in Fig. 1b. During this period, ionograms with 1-min intervals were obtained at Kazan (56.43°N, 58.56°E; epicentral distance 15,148 km), Russia. The difference between the epicentral distances for Obninsk and Kazan was approximately 773 km. The most significant MCS was observed at 0800 UTC, as shown in Fig. 1a. The mean propagation velocity of the Rayleigh waves along Earth's surface was estimated at 3.8 km/s (Maruyama et al. 2016a). Thus, it is estimated that the ground motion of the Rayleigh waves started at around 0740

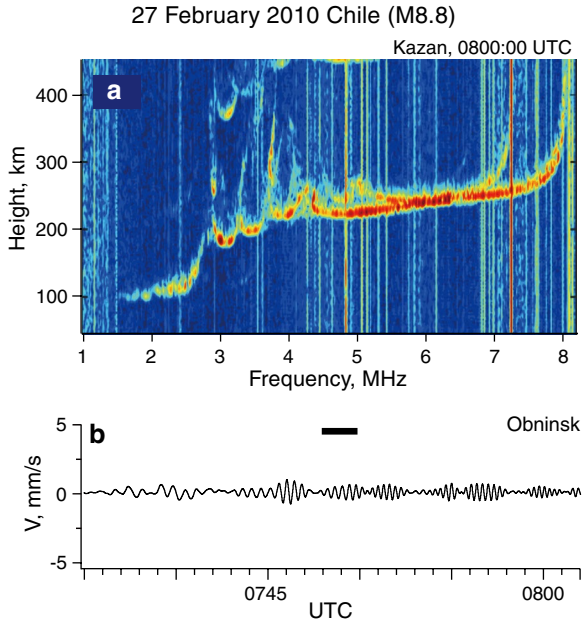

Fig. 1 Ionospheric disturbance caused by 2010 M8.8 Chile earthquake. **a** Ionogram showing multiple cusp signature observed at Kazan (epicentral distance 15,148 km), Russia, and **b** seismogram observed at Obninsk (epicentral distance 14,375 km), Russia

UTC at Kazan with a delay of ∼3 min after the occurrence at Obninsk. The ionospheric disturbances shown in Fig. 1a might be caused by the ground motion indicated by the horizontal bar in Fig. 1b, considering the Rayleigh wave propagation time from Obninsk to Kazan and the acoustic wave propagation time from the ground to the ionosphere at Kazan. The maximum amplitude of Rayleigh waves was observed at 0746 UTC at Obninsk. However, a deep amplitude modulation of the seismic signals was observed, as shown in Fig.1b. The modulation was most probably caused by multipathing and interference (Capon 1970), and the modulation pattern may not be the same at Kazan. It is natural to consider that the most significant MCS ionogram at Kazan, as shown in Fig. 1a, was caused by the largest amplitude of Rayleigh waves at a level similar to that at Obninsk (0.9 mm/s).

A similarly significant MCS was observed at Yamagawa (31.2°N, 130.62°E; epicentral distance 1124 km), Japan, after the M7.7 aftershock (36.12°N, 141.25°E; 0615:34 UTC) of the massive M9.0 Tohoku-Oki earthquake in 2011, as shown in Fig. 2a. The maximum amplitude of the Rayleigh wave responsible for this MCS was 5.0 mm/s at Tashiro (31.19°N, 130.91°E), near Yamagawa (difference in epicentral distances of 23 km), as shown by the horizontal bar at ∼ 0621:30 UTC in Fig. 2b. Figure 3a shows another example of an MCS ionogram observed at Yamagawa during the same earthquake. In this ionogram, the amplitude of the deformation was small, showing wiggles at frequencies of 3.5–6 MHz, which is almost the detection limit of coseismic ionogram deformation. Figure 3b shows the ground motion at Tashiro. The large-amplitude signals before ∼0556 UTC (goes off-scale in the plot) were the Rayleigh waves excited by the M9.0 main shock. The ground motion responsible for the MCS ionogram in Fig. 3a is shown by the horizontal bar in Fig. 3b and was most probably excited by the M6.6 aftershock at 0558 UTC; the amplitude was 0.5–1 mm/s. (Note that the ionosonde was operated at each quarter-hour and no ionogram corresponding to the main shock was obtained.)

When the three ionograms in Figs. 1a, 2a, and 3a after the two earthquakes are compared, it is found that ionograms at Kazan are likely to be roughly five times more susceptible to the seismic ground motion than those at Yamagawa. The two ionosonde sites are characterized by different dip angles: $I = 72°$ at Kazan and $I = 45°$ at Yamagawa.

Magnetic inclination effects

Neutral–ion coupling

The magnetic inclination effect on the wave-induced electron density perturbation was estimated by examining the ion continuity equation under the influence of the neutral particle motion of acoustic waves that propagate upward, as described below (Maruyama and Shinagawa 2014),

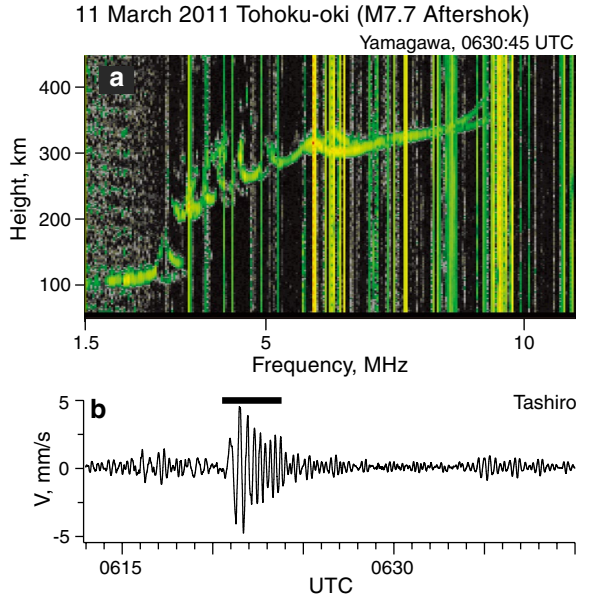

Fig. 2 Ionospheric disturbance caused by M7.7 aftershock of 2011 Tohoku-Oki earthquake. **a** Ionogram showing multiple cusp signature observed at Yamagawa (epicentral distance 1124 km), Japan, and **b** seismogram observed at Tashiro (epicentral distance 1101 km), Japan

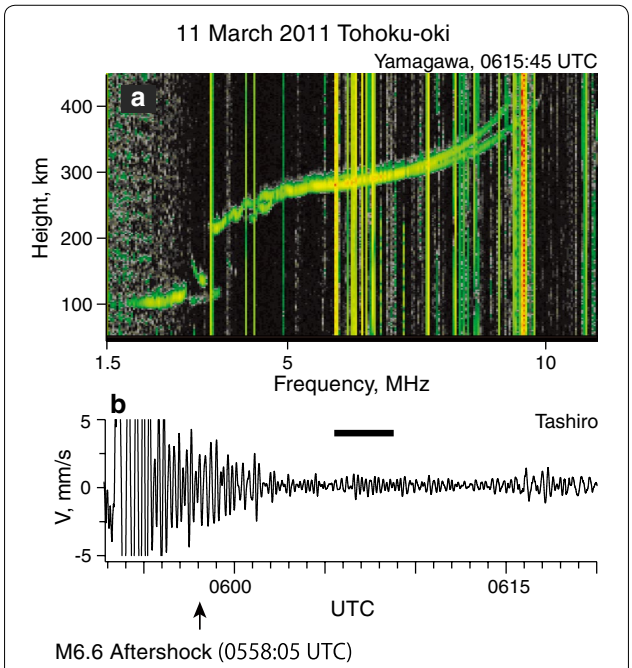

Fig. 3 Ionospheric disturbance caused by M6.6 aftershock of 2011 Tohoku-Oki earthquake. **a** Ionogram showing wiggles observed at Yamagawa (epicentral distance 1261 km), Japan, and **b** seismogram observed at Tashiro (epicentral distance 1240 km), Japan

$$\frac{\partial N_i}{\partial t} = -v_{\parallel} \sin I \frac{\partial N_i}{\partial z} - N_i \sin I \frac{\partial v_{\parallel}}{\partial z} + P_i - L_i \quad (1)$$

Here, t and z denote time and height, respectively. The ionosphere is treated as single-fluid collisional plasma containing a mixture of O^+ and NO^+, i.e., both ion species and electron have a common velocity, and N_i is the total ion density (equal to the electron density n_e). The ion is assumed to move at the velocity $v_{\parallel}$ along the magnetic field line with the dip angle I, P_i is the ion production rate by photoionization, and L_i is the ion loss rate due to the dissociative recombination of NO^+. The ion velocity $v_{\parallel}$ along the magnetic field line is given by

$$v_{\parallel} = -\frac{2 \sin I}{\sum_k m_k n_k \nu_{kn}} \frac{\partial p_i}{\partial z} - \frac{g}{\overline{\nu}_{in}} \sin I + u \sin I \quad (2)$$

In the denominator of the first term on the right-hand side of (2), the summation is over ion species k, and m_k is the ion mass, n_k is the ion density, and ν_{kn} is the ion–neutral collision frequency of O^+ ($k = 1$) and NO^+ ($k = 2$). The other parameter in the first term is p_i, the plasma pressure. In the second term, g is the magnitude of the gravitational acceleration and $\overline{\nu}_{in}$ represents the mean ion–neutral collision frequency. For each ion species, the sum of collision frequencies over the neutral species O, O_2, and N_2 was considered. The last term is the effect of the neutral particle motion with the vertical velocity u of acoustic waves. From (1) and (2), the rate of change in N_i owing to vertically propagating acoustic waves is proportional to $\sin^2 I$ and ionospheric disturbances larger by $\sin^2 72^\circ / \sin^2 45^\circ = 1.81$ are anticipated at Kazan than at Yamagawa for the same amplitude of acoustic waves.

Radio propagation

The magnetic inclination also affects the radio wave propagation. The virtual height $h'(f)$ measured using the ionosonde at the frequency f is given by

$$h'(f) = c \int_0^{h_r} \frac{dz}{v_g} = \int_0^{h_r} \mu'(f_p(z), f) dz \quad (3)$$

where h_r is the reflection level, $f_p(z)$ is the plasma frequency at the height z, and μ' is the group refractive index (the ratio between the speed of light c and the group velocity v_g), which is related to the refractive index μ described below by Appleton formula with negligible collisions (Davies 1969):

$$\mu^2 = 1 - \frac{2X(1-X)}{2(1-X) - Y_T^2 \pm \left[Y_T^4 + 4(1-X)^2 Y_L^2\right]^{1/2}} \quad (4)$$

$$\mu' \mu = \mu^2 + \frac{2}{D}\left[1 - \mu^2 - X^2 + \frac{(1-\mu^2)(1-X^2)Y_L^2}{A}\right] \quad (5)$$

$$X = \frac{f_p^2}{f^2} \quad (6)$$

$$D = 2(1-X) - Y_T^2 - A \quad (7)$$

$$A^2 = Y_T^4 + 4Y_L^2(1-X)^2 \quad (8)$$

$$Y = \frac{f_B}{f} \quad (9)$$

$$Y_L = Y \cos\theta \quad (10)$$

$$Y_T = Y \sin\theta \quad (11)$$

where f_B is the electron gyrofrequency and θ is the angle between the propagation vector and the magnetic field. For vertical incidence rays, $\theta = \pi/2 - I$. The + and − signs in Eq. (4) refer to the ordinary and extraordinary waves, respectively, and ordinary-mode propagation (μ'_+) is considered in this study.

The cusp signature in ionograms is ascribed to the increased propagation delay in a thin slab of plasma just below the reflection level ($X \approx 1$) when the electron density gradient is reduced (or the thickness of this slab increases) at the density ledge (Maruyama et al. 2016a) formed by an acoustic wave. The group refractive index near reflection is approximated as follows (Davies 1969) and was examined to estimate the magnetic inclination effect on the cusp signature.

$$\mu'_+ \approx (1-X)^{-1/2} \csc\theta \quad (12)$$

From this form, ionograms at Kazan are expected to be more sensitive to the density perturbation than those at Yamagawa by a factor of approximately $\csc 18^\circ / \csc 45^\circ = 2.29$.

The approximate formula (12) is not valid when θ comes close to zero or near the magnetic pole, where the propagation is quasi-longitudinal (Davies 1969). Exact calculations of μ'_+ from (4) to (11) are shown in Figs. 4 and 5. Figure 4 shows μ'_+ for various dip angles for $X \geq 0.97$. The calculation for Yamagawa ($I = 45^\circ$) is shown by the orange solid line, and those for other Japanese ionosonde sites from Okinawa to Wakkanai ($I = 38$–59°) are shown by the dotted lines. The calculation for Kazan ($I = 72^\circ$) is shown by the green solid line. The difference in the group refractive index is significant when X approaches 1, i.e., near the reflection level. Figure 5 shows μ'_+ for $X \approx 1$ for dip angles between 0° and

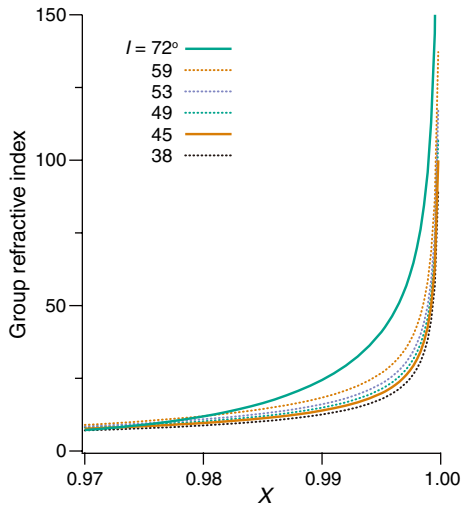

Fig. 4 Frequency dependence of group refractive index for different dip angles (I). Vertical incidence rays are assumed, and the angle between the ray direction and the magnetic field is $\pi/2 - I$

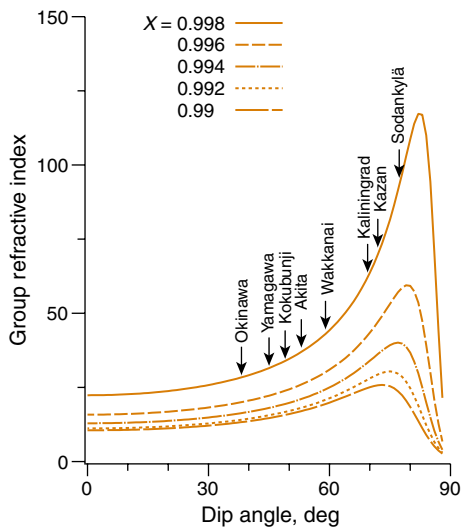

Fig. 5 Dip angle (I) dependence of group refractive index for different values of X ($= f_p^2/f^2$). Vertical incidence rays are assumed, and the angle between the ray direction and the magnetic field is $\pi/2 - I$. MCS ionograms were also observed at Kaliningrad, Russia, and Sodankylä, Finland, after the 2012 Sumatra earthquake (epicentral distances ~9000 km) (Yusupov and Akchurin 2015)

90° except for exactly the magnetic pole. The magnetic inclination effect on the cusp signature increases quickly above $I \sim 60°$. This behavior distinguishes Kazan from Japanese ionosonde sites.

Numerical simulations

The numerical study on the sensitivity of ionograms to atmosphere–ionosphere perturbation induced by ground motion followed two steps. The simulation of acoustic wave propagation and associated electron density perturbation was first conducted. Then ionograms were synthesized from the perturbed electron density distribution. The calculations were conducted for $I = 45$ and 72° corresponding to Yamagawa and Kazan, respectively.

The unperturbed electron density profile prior to the application of acoustic waves was obtained by integrating the plasma equation set (1) and (2) with a fixed local time, 1500 LT, until the equilibrium state was attained. This process ensures that the background electron density distribution does not change during the simulation of acoustic wave propagation. Because our major purpose is to examine the effect of magnetic inclination at two locations with different dip angles, background atmospheric parameters and solar zenith angles for both calculations were chosen to be the same as those at Yamagawa when coseismic disturbances were observed after the M9.0 Tohoku-Oki earthquake in 2011, and only I was changed with the locations. In actual situations, the ionosphere and thermosphere vary widely depending on the local time, latitude, season, solar activity, etc. A key parameter for the detection of MCS in ionograms is the f_oF_1 (Maruyama et al. 2012), which is a measure of the vertical electron density gradient in the lower F region. The f_oF_1 in the two cases (Kazan and Yamagawa) were very similar (4–5 MHz). It is possible to include the above factors in the numerical calculations, but an essential physical mechanism will be obscure. Figure 6 shows the resultant unperturbed density profiles for $I = 45$ and 72° by the green and orange lines, respectively. In the plots, the electron densities at the peak and in the topside for $I = 72°$ were lower than those for $I = 45°$, which is ascribed to the difference in the vertical component of the field-aligned diffusion that depends on the dip angle.

The neutral particle motion of the acoustic wave was obtained by solving the following equation set (Maruyama and Shinagawa 2014).

$$\frac{\partial \rho}{\partial t} = -u\frac{\partial \rho}{\partial z} - \rho\frac{\partial u}{\partial z} \tag{13}$$

$$\frac{\partial u}{\partial t} = -u\frac{\partial u}{\partial z} - \frac{1}{\rho}\frac{\partial p}{\partial z} - g + \frac{1}{\rho}\frac{\partial}{\partial z}\left(\eta\frac{\partial u}{\partial z}\right) \tag{14}$$

$$\frac{\partial T}{\partial t} = -u\frac{\partial T}{\partial z} - \frac{RT}{c_v}\frac{\partial u}{\partial z} + \frac{1}{\rho c_v}\frac{\partial}{\partial z}\left(\kappa\frac{\partial T}{\partial z}\right) + \frac{Q}{c_v} \tag{15}$$

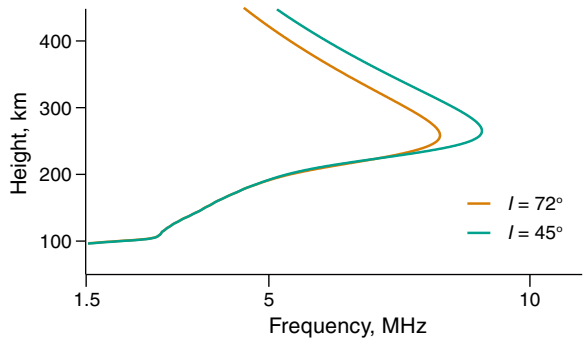

Fig. 6 Unperturbed ionospheric profiles used for simulation of acoustic wave-induced anomaly for $I = 72°$ (*orange*) and 45° (*green*)

$$p = \rho RT \tag{16}$$

Here, t and z denote time and height, respectively, ρ is the mass density, u is the vertical particle velocity, p is the pressure, g is the magnitude of the gravitational acceleration, η is the molecular viscosity, T is the temperature, R is the gas constant, c_v is the specific heat at constant volume, κ is the thermal conduction coefficient, and Q is the net heating rate. The coefficients of molecular viscosity, specific heat, and thermal conduction were taken from the formulae given by Rees (1989). In the momentum equation (14), the momentum transfer from ion motion to neutral motion is neglected because it is much smaller than the other terms. The initial state of the atmosphere was specified by the MSISE90 model (Hedin 1991) and assumed to be in equilibrium. In the thermodynamic equation (15), Q was determined to satisfy thermal equilibrium ($\partial T/\partial t = 0$) before perturbation was applied to the neutral atmosphere ($u = 0$), which contains the heat source due to absorption of solar ultraviolet and extreme ultraviolet radiations and the heat loss due to cooling by infrared radiation.

The initial amplitude of atmospheric motion just above the ground was assumed to take a sinusoidal form with an amplitude of 0.5 mm/s and a period of 24 s and is expressed as

$$u_0(t) = a_0 \sin\left(2\pi \frac{t}{\tau}\right) \tag{17}$$

Figure 7 shows the vertical velocity of the neutral particle associated with the propagation of the acoustic waves. Because the atmospheric parameters were the same for the two calculations and the ion-drag effect on the neutral particle dynamics was neglected, velocities were identical for $I = 45$ and 72°. The amplitude increased with height and became visible above ~50 km in the diagram. However, it reached the maximum value of approximately 6 m/s at a height of 170 km, i.e., 1.2×10^4 times

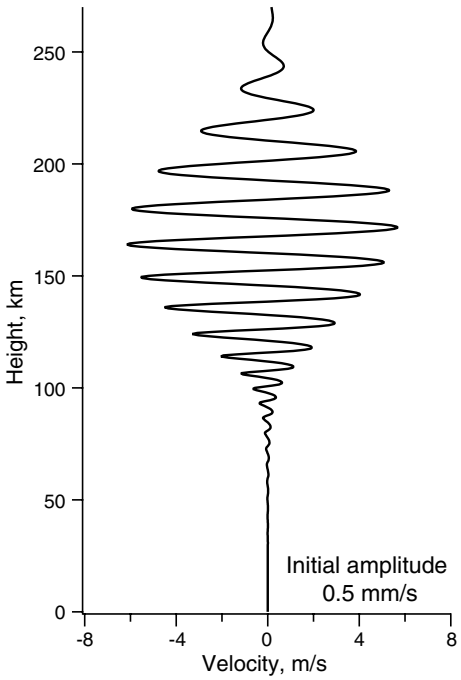

Fig. 7 Amplitude of acoustic wave propagating upward

the initial value on the ground. At higher altitudes, the wave amplitude decayed with height mostly as a result of viscous damping and almost vanished above the F_2 peak height. Figure 8 shows the percent electron density perturbation for $I = 45$ and 72° by the green and orange lines, respectively. The amplitude of positive perturbation (enhancement) reached a maximum of ~0.40 and ~0.74% for $I = 45$ and 72°, respectively, near 172 km. Similarly, the amplitude of negative perturbation (depletion) reached a maximum of ~0.46 and ~0.84% for $I = 45$ and 72°, respectively, near 165 km. It is noted that the negative half cycle is slightly shorter than the positive half cycle and the net gain or loss of plasma through one cycle of perturbation is nil. The inclination effect on the neutral–ion coupling became visible, and the overall maximum amplitude of the density perturbation for $I = 72°$ (Kazan) was ~1.8 times that for $I = 45°$ (Yamagawa), as expected from (1) and (2).

Finally, ionograms were synthesized from the perturbed electron density profiles by calculating virtual heights at frequencies in 0.02-MHz increments, as described by (3)–(11). In this calculation, only O-mode propagation in the vertical direction was considered, and the frequency increments were in accord with the ionosonde operation. Figure 9 shows the ionograms for $I = 45$ and 72° in green and orange, respectively, and the plot for $I = 72°$ is shifted by 30 km. The two ionograms show different responses to the atmosphere–ionosphere

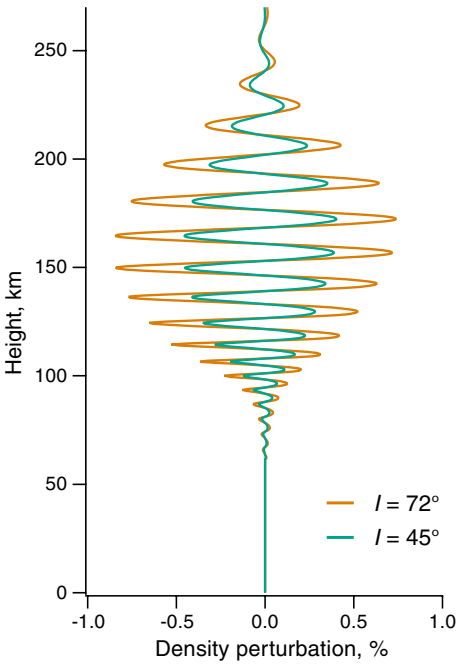

Fig. 8 Perturbation amplitude as a percentage of the background electron density induced by acoustic waves for $I = 72°$ (*orange*) and 45° (*green*)

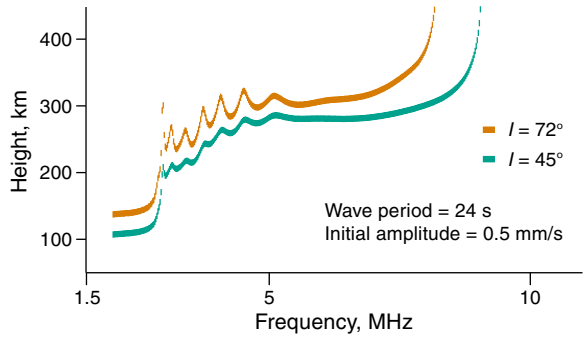

Fig. 9 Synthesized ionograms (*O*-mode only) for $I = 72°$ (*orange*) and 45° (*green*) corresponding to ionospheric disturbances in Fig. 8. The virtual height at each frequency is plotted by a symbol " | " representing the sounder pulse width so that the plots look like actual ionograms

perturbations induced by the same amplitude of seismic ground motion. The disturbance in the trace for $I = 72°$ exhibits a well-developed cusp signature, while that for $I = 45°$ merely shows wiggles. The ratio of cusp heights was ~3, which was slightly smaller than the combination of two geometrical effects (1.81×2.29).

Summary

Seismic waves cause ionospheric disturbances at remote distances. Rayleigh waves with a period of 15–50 s induce multiple cusp signatures (MCSs) or wiggles in ionogram traces. In the previous observations, this type of irregularity was found to be significant at higher latitudes, such as Kazan, Russia, than Japan's latitudes. By numerical simulations, it was shown that the sensitivity of ionograms to seismic ground motion varies depending on the magnetic inclination. At higher latitudes with a large dip angle, coupling between the acoustic waves launched by seismic ground motion and the ionospheric plasma is strong, inducing a large amplitude of perturbation in the electron density than that at lower latitudes with a small dip angle. Radio pulses transmitted by ionosondes are sensitive to the electron density perturbation at a small angle between the ray direction and the magnetic fields at higher latitudes. Thus, the combined effect of atmosphere–ionosphere coupling and radio wave propagation at high latitudes yields a high sensitivity of the ionosonde detection of seismic ground motion, which explains the observations of coseismic ionospheric irregularities at a large epicentral distance of 15,000 km such as at Kazan, after the 2010 Chile earthquake.

Authors' contributions

TM analyzed the ionograms and seismograms and synthesized the ionograms. HS simulated atmosphere–ionosphere coupling. KY and AA developed and operated the ionosonde at Kazan and searched MCS ionograms at long distances from epicenters. All authors read and approved the final manuscript.

Author details

[1] National Institute of Information and Communications Technology, 2-1 Nukuikita 4-chome, Koganei, Tokyo 184-8795, Japan. [2] Kazan Federal University, 18 Kremlyovskaya St., Kazan, Russian Federation 420008.

Acknowledgements

Broadband seismograms were obtained from the National Research Institute for Earth Science and Disaster Prevention (NIED), Japan, and Incorporated Research Institutions for Seismology (IRIS). The work at Kazan Federal University was performed in accordance with the Russian Government Program of Competitive Growth of Kazan Federal University.

Competing interests

The authors declare that they have no competing interests.

Received: 1 October 2016 Accepted: 11 January 2017
Published online: 30 January 2017

References

Artru J, Farges T, Lognonné P (2004) Acoustic waves generated from seismic surface waves: propagation properties determined from Doppler sounding observations and normal-mode modelling. Geophys J Int 158:1067–1077

Berngardt OI, Kotovich GV, Mikhailov SY, Podlesnyi AV (2015) Dynamics of vertical ionospheric inhomogeneities over Irkutsk during 06:00–06:20 UT 11/03/2011 caused by Tohoku earthquake. J Atmos Solar Terr Phys 132:106–115

Calais E, Minster JB (1995) GPS detection of ionospheric perturbations following the January 17, 1994, Northridge earthquake. Geophys Res Lett 22(9):1045–1048

Capon J (1970) Analysis of Rayleigh-wave multipath propagation at LASA. Bull Seism Soc Am 60(5):1701–1731

Chum J, Hruska F, Zednik J, Lastovicka J (2012) Ionospheric disturbances (infrasound waves) over the Czech Republic excited by the 2011 Tohoku earthquake. J Geophys Res 117:A08319. doi:10.1029/2012JA017767

Chum J, Liu JY, Laštovička J, Fišer J, Mošna Z, Baše J, Sun YY (2016) Ionospheric signatures of the April 25, 2015 Nepal earthquake and the relative role of compression and advection for Doppler sounding of infrasound in the ionosphere. Earth Planets Space 68:24. doi:10.1186/s40623-016-0401-9

Davies K (1969) Ionospheric radio waves. Blaisdell Publishing Company, Waltham

Hedin AE (1991) Extension of the MSIS Thermosphere Model into the middle and lower atmosphere. J Geophys Res 96(A2):1159–1172. doi:10.1029/90JA02125

Lay T, Wallace TC (1995) Modern global seismology. Academic Press, San Diego

Leonard RS, Barnes RA (1965) Observation of ionospheric disturbances following the Alaska earthquake. J Geophys Res 70(5):1250–1253

Liu JY, Sun YY (2011) Seismo-traveling ionospheric disturbances of ionograms observed during the 2011 M_w 9.0 Tohoku Earthquake. Earth Planets Space 63:897–902

Liu JY, Chen CH, Sun YY, Chen CH, Tsai HF, Yen HY, Chum J, Lastovicka J, Yang QS, Chen WS, Wen S (2016) The vertical propagation of disturbances triggered by seismic waves of the 11 March 2011 M9.0 Tohoku earthquake over Taiwan. Geophys Res Let 43. doi:10.1002/2015GL067487

Maruyama T, Shinagawa H (2014) Infrasonic sounds excited by seismic waves of the 2011 Tohoku-oki earthquake as visualized in ionograms. J Geophys Res 119:4094–4108. doi:10.1002/2013JA019707

Maruyama T, Tsugawa T, Kato H, Saito A, Otsuka Y, Nishioka M (2011) Ionospheric multiple stratifications and irregularities induced by the 2011 off the Pacific coast of Tohoku Earthquake. Earth Planets Space 63:869–873

Maruyama T, Tsugawa T, Kato H, Ishii M, Nishioka M (2012) Rayleigh wave signature in ionograms induced by strong earthquakes. J Geophys Res 117:A08306. doi:10.1029/2012JA017952

Maruyama T, Yusupov K, Akchurin A (2016a) Ionosonde tracking of infrasound wavefronts in the thermosphere launched by seismic waves after the 2010 M8.8 Chile earthquake. J Geophys Res Space Phys 121:2683–2692. doi:10.1002/2015JA022260

Maruyama T, Yusupov K, Akchurin A (2016b) Interpretation of deformed ionograms induced by vertical ground motion of seismic Rayleigh waves and infrasound in the thermosphere. Ann Geophys 34:271–278. doi:10.5194/angeo-34-271-2016

Nishitani N, Ogawa T, Otsuka Y, Hosokawa K, Hori T (2011) Propagation of large amplitude ionospheric disturbances with velocity dispersion observed by the SuperDARN Hokkaido radar after the 2011 off the Pacific coast of Tohoku Earthquake. Earth Planets Space 63:891–896

Ogawa T, Nishitani N, Tsugawa T, Shiokawa K (2012) Giant ionospheric disturbances observed with the SuperDARN Hokkaido HF radar and GPS network after the 2011 Tohoku earthquake. Earth Planets Space 64:1295–1307

Rees MH (1989) Physics and chemistry of the upper atmosphere. Cambridge University Press, Cambridge

Rolland LM, Lognonné P, Astafyeva E, Kherani EA, Kobayashi N, Mann M, Munekane H (2011) The resonant response of the ionosphere imaged after the 2011 off the Pacific coast of Tohoku Earthquake. Earth Planets Space 63:853–857

Tanaka T, Ichinose T, Okuzawa T, Shibata T, Sato Y, Nagasawa C, Ogawa T (1984) HF-Doppler observations of acoustic waves excited by the Urakawa-Oki earthquake on 21 March 1982. J Atmos Terr Phys 46(3):233–245

Tsugawa T, Saito A, Otsuka Y, Nishioka M, Maruyama T, Kato H, Nagatsuma T, Murata KT (2011) Ionospheric disturbances detected by GPS total electron content observation after the 2011 off the Pacific coast of Tohoku Earthquake. Earth Planets Space 63:875–879

Wolcott JH, Simons DJ, Lee DD, Nelson RA (1984) Observations of an ionospheric perturbation arising from the Coalinga earthquake of May 2, 1983. J Geophys Res 89(A8):6835–6839

Yuen PC, Weaver PF, Suzuki RK, Furumoto AS (1969) Continuous, traveling coupling between seismic waves and the ionosphere evident in May 1968 Japan earthquake data. J Geophys Res 74(9):2256–2264

Yusupov K, Akchurin A (2015) Incredibly distant ionospheric responses to earthquake. Geophys Res Abs 17:EGU2015-15198-1